Generation of 565 MW of *X*-band power using a metamaterial power extractor for structure-based wakefield acceleration

Julian Picard,* Ivan Mastovsky, Michael A. Shapiro, and Richard J. Temkin
Massachusetts Institute of Technology, Cambridge, Massachusetts 02139, USA

Xueying Lu†
Northern Illinois University, DeKalb, Illinois 60115, USA

Manoel Conde, D. Scott Doran, Gwanghui Ha, John G. Power, Jiahang Shao, and Eric E. Wisniewski
Argonne National Laboratory, Lemont, Illinois 60439, USA

Chunguang Jing
Euclid Techlabs LLC, Solon, Ohio 44139, USA

(Received 11 December 2021; accepted 14 April 2022; published 16 May 2022)

We report the generation of up to 565 MW, 2.7 ns (FWHM) pulses at 11.7 GHz from a metamaterial structure in test at the Argonne Wakefield Accelerator. The highest power was generated by a train of eight 65 MeV electron bunches spaced at 1.3 GHz with a total charge of 355 nC. The metamaterial structure consists of 100 copper unit cells each consisting of a wagon-wheel plate and a spacer plate with a total structure length of 0.2 m. The 565 MW pulse generates a wakefield with a peak on-axis gradient of 135 MV/m that could be used to accelerate a trailing main bunch. An estimated surface electric field of over 1 GV/m is generated on the metamaterial plates at the peak power level but no evidence of breakdown was observed during testing. Tests with single electron bunches and with trains of bunches of up to 100 nC produced output power levels in excellent agreement with simulations. At higher total bunch charge, offsets of the bunches from the axis resulted in beam interception and reduced output power. Simulations indicate that a perfectly aligned bunch train would generate more than 1 GW of power from the structure.

DOI: 10.1103/PhysRevAccelBeams.25.051301

I. INTRODUCTION

Wakefield acceleration seeks to overcome the limitations of traditional accelerator schemes to enable smaller and more energetic beamlines and colliders [1–3]. The primary limitation of traditional acceleration schemes is the risk of RF breakdown, which has limited achievable accelerating gradients to around 120 MV/m in multicell structures [4,5], 200 MV/m for single-cell structures [6], and 250 MV/m in cryogenic single-cell [7] and high-frequency structures [8]. Evidence suggests that the risk of breakdown decreases exponentially with rf pulse width [9]. As such, exploring methods of acceleration that employ short rf pulses may be a promising path to high gradients.

One type of wakefield acceleration scheme pushing toward higher accelerating gradients by using short rf pulse widths is structure-based wakefield acceleration, or SWFA [10–16,16–24]. One promising type of SWFA is the two-beam acceleration scheme (TBA). The TBA scheme can be seen in Fig. 1. First, a high charge drive bunch is passed through a dedicated power extractor structure. The power extractor is specifically designed to convert energy from the drive beam into a microwave pulse. The resulting rf can then be passed through a waveguide to a separate acceleration structure, where it can be used to accelerate a low charge main beam. TBA has several advantages over other SWFA acceleration schemes, including the ability to independently tune the beamlines for the drive and main bunches and allowing for the uncoupled optimization of the power extractor and acceleration structures.

Two concepts have been proposed for a next-generation 3 TeV linear collider based on the two-beam SWFA scheme. The Compact Linear Collider (CLIC), developed at CERN, employs 230 ns rf pulses to generate accelerating

*jpicard@mit.edu
†Also at Argonne National Laboratory, Lemont, Illinois 60439, USA.

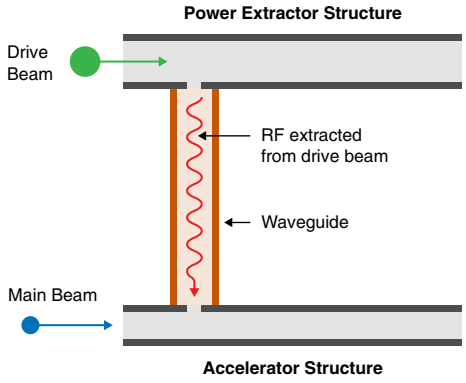

FIG. 1. Schematic of two-beam structure-based wakefield acceleration. Rf power is generated from a drive beam (green) by the power extractor structure. This rf pulse is transported through a waveguide to a separate accelerator structure, where the main beam (blue) is accelerated.

gradients up to 100 MV/m [25,26]. The other proposal is the Argonne Flexible Linear Collider (AFLC), designed at Argonne National Lab, which utilizes much shorter (< 25 ns) rf pulses [16,19,27]. The AFLC seeks to capitalize on the expected benefits of short-pulse acceleration to achieve gradients as high as 270 MV/m.

This work presents the design of a power extractor that has been optimized using metamaterials to generate the very short high power pulses required for the AFLC concept. Metamaterials (MTM) are artificial structures assembled from arrays of subwavelength unit cells. The material thus appears homogeneous or semihomogeneous to electromagnetic waves in a specific frequency range. By tailoring the parameters of the unit cell, the macroscopic material can be designed to exhibit electromagnetic behaviors not found in normal materials. Double-negative metamaterials, a specific category of metamaterials, are of particular interest because they possess an effective permittivity and permeability that are simultaneously negative in the frequency band of interest [28]. A unique behavior of double-negative materials is that they exhibit reverse Cherenkov radiation [29–31]. In general, a charged particle traveling faster than the phase velocity of light in a medium will coherently radiate Cherenkov radiation. In a normal (ϵ, $\mu > 0$) material, this radiation propagates such that the longitudinal component of both phase and group velocity in the same direction as the particle velocity. In a double-negative metamaterial, the radiation propagates with a negative group velocity—backwards relative to the particle velocity. This reverse Cherenkov radiation has the property that the longitudinal component of the phase velocity is still positive, parallel to the particle movement. Double-negative metamaterials have been successfully demonstrated as promising candidates for rf power generation [32–38]. The power extractor design presented in this paper uses a custom metamaterial, described in Sec. II A, to generate high power in the form of reverse Cherenkov radiation.

The application of metamaterials to a power extractor discussed in this work is among a variety of power extractor designs proposed and tested at the 65 MeV Argonne Wakefield Accelerator (AWA) beamline in efforts toward the AFLC. Concepts include photonic bandgap structures [39–41], dielectric-loaded waveguides [10–12,17], metallic disk-loaded waveguide structures [42], dielectric disk-loaded waveguide structures [43] and others [18,44,45]. Metamaterial structures offer unique advantages in comparison to other options [46]. First, the sub-wavelength design allows for a simultaneously-high group velocity and shunt impedance, enabling a higher power generation efficiency than other designs. Second, because the interaction is dictated by the design of the sub-wavelength unit cell, there is a high degree of flexibility in customizing the beam-structure interaction by manipulating the cell dimensions. Finally, the metallic structure is simple to manufacture and resistant to thermal and beam-driven damage.

Two direct precursor experiments based on MTM structures have been designed and built at MIT and tested using the AWA beamline. These experiments provided a foundation for this work by demonstrating the viability of a metamaterial-based power extractor for SWFA. The Stage I experiment in 2018 utilized 40 metamaterial unit cells to generate 80 MW of 11.4 GHz power [46]. The Stage II experiment in 2019 used 100 cells to generate 380 MW of 11.7 GHz power [47]. During the Stage II experiment, the power generated was substantially below the design value and beam transmission through the structure was difficult.

The Stage III experiment presented in this paper implements substantial design changes to improve power generation efficiency and beam transmission. These improvements include an all-copper construction to minimize rf loss, a high-power symmetric coupler to increase output power and beam transmission, and a treatment of the metamaterial structure to reduce the risk of rf breakdown. In aggregate, these improvements increase the output power generation efficiency by 75% over the previous Stage I and Stage II iterations.

II. METAMATERIAL STRUCTURE DESIGN

The Stage III metamaterial-based power extractor presented in this work consists of 100 metamaterial cells compressed between forward and backward output couplers. The design of the metamaterial is described in the forthcoming section, along with the significant improvements made in the Stage III structure.

A. Wagon wheel metamaterial

A custom metamaterial, termed the wagon wheel metamaterial, was designed at MIT specifically for application as a power extractor [46]. An exploded view of two unit cells of the wagon wheel structure are shown in Fig. 2. Each cell has a period of 2 mm and consists of one structure plate

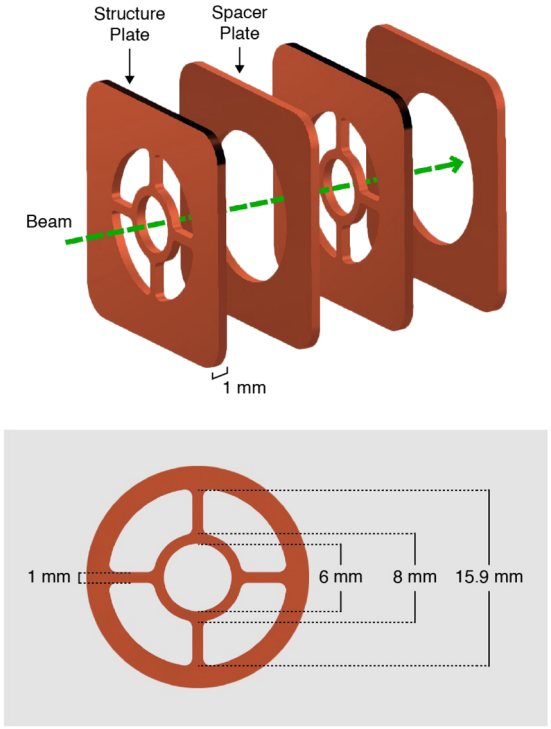

FIG. 2. Top: exploded view of two wagon wheel metamaterial unit cells. Each cell consists of a structure plate and a spacer plate, each 1 mm in thickness. A beam traversing the center of the cells will radiate backwards in reverse Cherenkov radiation. Bottom: dimensions of the wagon wheel structure plate.

and one spacer plate of equal thickness. The wagon wheel metamaterial is a double-negative metamaterial. The negative permeability is provided by the circular waveguide operating in a TM-like mode below cutoff [28] and the negative permeability is provided by the structure loading within the waveguide [48]. When a charge passes through the center of the structure, it radiates reverse Cherenkov radiation with a negative group velocity. This is evidenced by the negative slope of the metamaterial's dispersion curve at the interaction point in Fig. 3. The structure is designed such that the interaction frequency with the highly relativistic electron beam is at 11.7 GHz.

Backward traveling modes are also supported by traditional magnetically-coupled cavity structures [49]. The subwavelength nature of the metamaterial, however, allows for optimization of properties such as shunt impedance and rf group velocity beyond the capability of traditional coupled-cavity structures (see Table I). The distinction between traditional cavity-based structures and metamaterial-based structures for accelerator applications is discussed extensively in [50]. More details about the wagon wheel metamaterial specifically can be found in [51] and [52].

The power generated by a power extractor, $P(t)$, from a bunch with charge q is given by

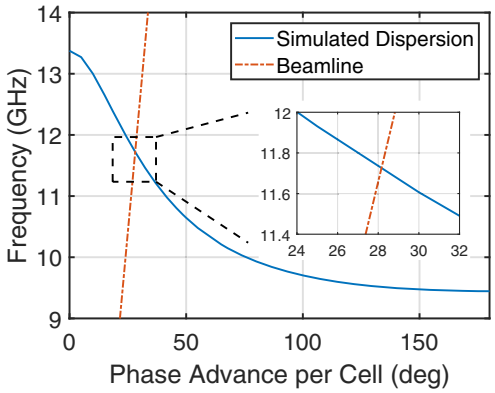

FIG. 3. Simulated dispersion curve for the wagon wheel metamaterial. The rf generated by the interaction with the beam will be at the frequency determined by the intersection of the dispersion curve and the beamline.

$$P(t) = q^2\left(\frac{\omega r_s}{4Q}\right)|v_g|\left(\frac{1}{1-|v_g|/c}\right)^2\Phi^2 e^{-2\alpha_0|v_g|t} \quad (1)$$

where ω is the interaction frequency, r_s is the shunt impedance per unit length, Q and v_g are the quality factor and group velocity of the considered mode, and $\Phi = \exp[-(k_z\sigma_z)^2/2]$ is the bunch form factor [12]. Note that $\Phi = 0.96$ for the wagon wheel structure [46]. In the time-dependent exponential term, α_0 is the electric field loss per unit length in the structure. The on-axis accelerating gradient can be calculated for a output power P by [49]:

$$E_{\mathrm{acc}} = \sqrt{\frac{\omega}{|v_g|}\left(\frac{r_s}{Q}\right)P_{\mathrm{out}}}. \quad (2)$$

From Eq. (1), it can be seen that simultaneously having a high group velocity and shunt impedance will maximize the output power. Generally, a high shunt impedance is achieved by minimizing the beam tunnel radius at the expense of the group velocity and ease of beam transmission. In comparison to other structures, the metamaterial structure allows for both a high shunt impedance and

TABLE I. Recent and proposed X-band power extractor concepts, demonstrating the simultaneously high r/Q and group velocity of the metamaterial structure.

Structure	Beam tunnel radius (mm)	r/Q (kΩ/m)	v_g
Wagon wheel MTM	3	21.2	−0.155c
Metallic DLWG [53]	3.05	14	0.0114c
Dielectric tube [23]	3.1	11.9	0.184c
Dielectric tube [23]	7.5	4.32	0.2c
Metallic DLWG [42,54]	8.8	3.92	0.22c

high group velocity with a reasonably sized beam tunnel. A parameter comparison of recent and proposed X-band experiments using the AWA facility can be seen in Table I.

The rf pulse generated by a single bunch has a width t_p which depends on the structure parameters. Because the bunches radiate backwards in the MTM structure, t_p is given by the sum of the bunch transit time through the structure and the propagation time of the rf pulse: $t_p = L/c + L/|v_g|$ where L is the structure length. For a 100-cell metamaterial structure with $L = 200$ mm, $t_p = 5$ ns.

The Argonne Wakefield Accelerator (AWA) can generate trains of 65 MeV bunches at the 1.3 GHz L-band frequency of the linear accelerators. By designing a power extractor to operate at a harmonic of this frequency (in this case the ninth harmonic, 11.7 GHz), the radiation from multiple bunches can be coherently added to increase the output power from the device. The peak output power can be increased by constructively interfering the rf from additional bunches until reaching the bunch ceiling, $N_c = \text{ceiling}(t_p/t_b)$, where t_b is the temporal bunch spacing. N_c is the number of bunches after which the pulse from the first bunch has fully exited the structure. Additional bunches establish a flat-top rather than increasing the peak power [12,23]. For the 1.3 GHz bunch frequency of the AWA beamline, $t_b = 769$ ps. A power extractor utilizing 100 cells of the wagon wheel metamaterial thus has $N_c = 7$ bunches. The above analysis assumes perfect square pulses. Because of the nonzero decay time of the individual rf pulses, additional power can still be achieved in experiment by adding an eighth bunch. This effect has been verified in both simulation and prior experiment.

B. All-copper construction

One primary improvement in the Stage III structure is the implementation of an all-copper construction to increase output power generation efficiency. The structure plates in the Stage I and Stage II experiments were constructed of stainless steel to reduce the risk of deformation or damage to the metamaterial structure, which would be much higher for a softer material such as copper. Because the nominal conductivity of steel is substantially lower than that of copper ($1.7e6\ S/m$ in comparison to $5.8e7\ S/m$), the steel plates were a substantial source of rf loss in the first two experiments. Eigenmode simulations of the wagon wheel unit cell constructed from a single material indicate that 85% of rf power loss in the cell is in the structure plates, in comparison to 15% in the spacer plates. The effect on the overall rf loss in the structure can be seen in Table II, which compares the electric field decay factor α_0 and quality factor between assemblies in which the structure plate material is either copper or steel.

In order to reduce the rf loss and increase output power, both the structure and spacer plates were manufactured from OFHC copper in the Stage III experiment. Given the concern over damage during manufacturing, measures were taken to ensure careful handling during wire EDM manufacturing and assembly. These methods, including individual plate handling and surface-protecting plastic film, were largely successful. Residual surface defects were mitigated using the process described in the Appendix. The resulting Stage III structure showed dramatically decreased insertion loss in comparison to the Stage II experiment. This can be seen in Fig. 4, with a 5 dB increase in S_{21} at the 11.7 GHz interaction frequency. As a result of the decreased rf loss, the 100-cell Stage III structure is predicted to generate 50% higher output power than the Stage II structure from the same eight bunch train.

TABLE II. Comparing the field decay factor and quality factor (for the fundamental mode) of a steel and copper metamaterial structure.

Structure plate material	α_0 (m^{-1})	Q
Copper	0.33	2400
Steel	3.0	260

C. Symmetric high-power coupler

After assessing the results of the Stage II experiment, it was discovered through CST particle-in-cell (PIC) simulations that bunches entering the structure on-axis were being deflected downwards. The extent of the deflection grew with output power, approaching deflections of 1° at peak power levels. It was initially assumed that this was due to the excitation of the dipole mode of the metamaterial structure. This higher-order mode, at a frequency near 17 GHz, was observed in the Stage II experiment, excited by bunches intentionally injected into the structure at an angle to the beam axis. Attempts at damping the dipole mode did not improve the deflection, however. Additional analysis found that the cause was instead due to dipole components of the fundamental mode, driven by the asymmetry of the high power output coupler.

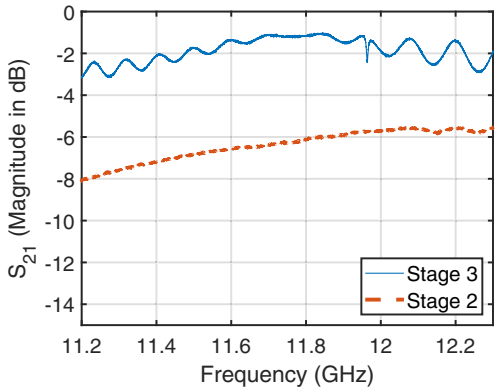

FIG. 4. Comparison of S_{21} measurements showing the reduction in transmission loss in the Stage III experiment.

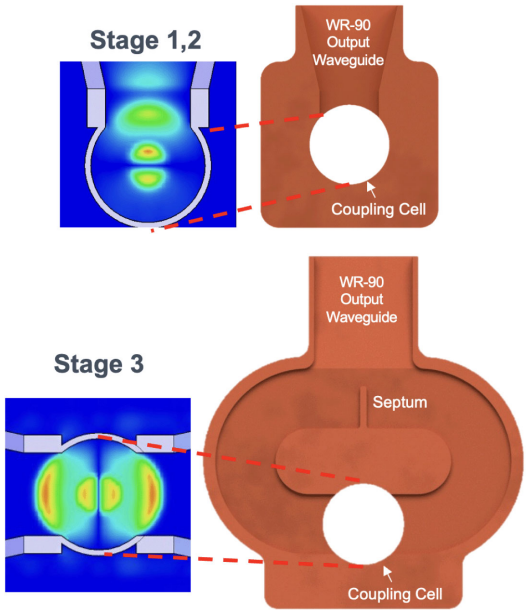

FIG. 5. The asymmetric coupler in the Stage I/II experiments (top right) generated a vertically-asymmetric mode in the coupling cell (top left). The symmetric coupler implemented in the Stage III experiment (bottom right) eliminated this asymmetric mode (bottom left) and the associated transverse kick. The field plots show the normalized magnitude of E_y and E_x, respectively.

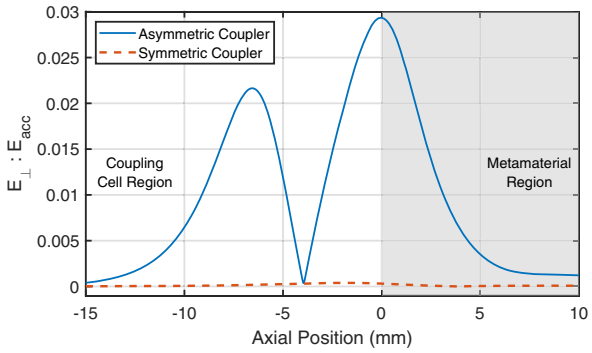

FIG. 6. The asymmetric mode in the Stage I/II coupling cell generated transverse electric field components in the fundamental mode. The magnitude of the deflecting field normalized to the accelerating gradient is shown in solid blue for the asymmetric design. The symmetry of the Stage III coupler eliminates this transverse field, as shown in dashed red.

The design of the high-power output coupler used in the Stage I/II experiments can be seen at top right in Fig. 5. The coupling cell converts the power radiated by the bunches in the metamaterial region from a TM-like mode to a standard TE mode of the WR-90 output waveguide. The backward propagation of the reverse Cherenkov radiation mode means that bunches entering the structure are immediately exposed to the fields within the high power coupling cell. The vertically-asymmetric design was originally chosen for simplicity and due to constraints in the experimental setup. However, this asymmetry forces the profile of the fundamental 11.7 GHz mode in the coupling cell to be asymmetric as well, as shown at top left in Fig. 5. Because this asymmetric mode has transverse components on-axis, bunches entering on-axis experience a transverse deflecting field. The extent of the effect is characterized in Fig. 6. With expected on-axis field gradients in excess of 100 MV/m, transverse gradients may be on the order of several MV/m in the coupling cell.

An effort was made to develop a symmetric high power output coupler. The result can be seen at bottom right in Fig. 5, in which the coupling cell is both horizontally and vertically symmetric. This was achieved by allowing for two independent output ports from the coupling cell, each with a slot thickness optimized to keep reflection of power from the MTM section below −20 dB. The result is a fully-symmetric coupling cell mode at the 11.7 GHz fundamental frequency. The magnitude of the on-axis deflecting fields was reduced by almost two orders of magnitude, as shown in Fig. 6.

Experimental constraints required an in-vacuum high power combiner to be developed to join the two output ports from the coupling cell to WR-90 waveguide. A racetrack-style design was implemented, with radii and septum dimensions tuned to minimize reflection [55]. To minimize design complexity, the up-taper to fundamental waveguide was altered to be in only one dimension, rather than the two-dimensional taper in the Stage I/II coupler design. The output combiner was manufactured in a split-block fashion by Vacuum Process Engineering, Inc. with three alternating machining/vacuum brazing cycles.

The symmetrized coupler design allows bunches injected into the structure on-axis to stay on axis, increasing the calculated output power by 15% for a given charge. As importantly, bunches injected into the structure slightly off-axis produce more output power than with the asymmetric coupler design. Figure 7 compares the normalized output power generated by each coupler design when driven by an eight bunch train injected into the structure 1 mm off-axis. The symmetric coupler produces 60% higher peak power and 40% higher pulse energy by reducing beam interception such that bunches contribute more of their energy to the output pulse.

A CAD representation of the full Stage III design is shown in Fig. 8. The asymmetric design was maintained for the low power forward coupler for several reasons. Experimental constraints were such that the increase in coupler height due to symmetrization would necessitate a different vacuum setup, which was impractical. In addition, the power in the forward coupler is very low, and any nonzero transverse gradient only affects the bunches as they leave the structure.

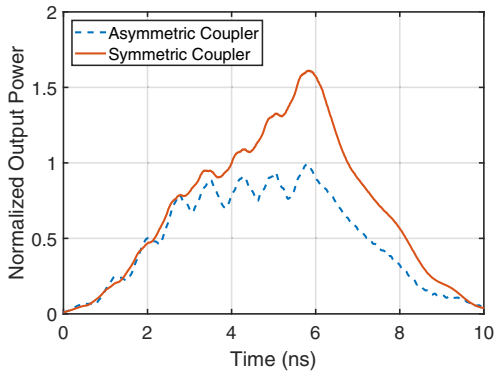

FIG. 7. The symmetric coupler design improves structure performance for a misaligned beam. For a set of 8 bunches centered 1 mm off-axis, the symmetric coupler (solid trace) produces 1.6x higher peak power and 1.4x more pulse energy than the asymmetric coupler design (dashed trace) by helping maintain linear bunch trajectory.

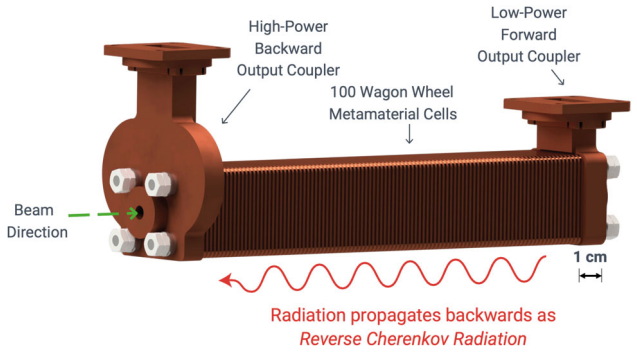

FIG. 8. A CAD model of the Stage III structure, including symmetric high power output coupler and asymmetric low-power forward coupler.

D. Peak surface electric field calculation

In standard accelerator cells that operate with hundreds of nanoseconds or longer rf pulses, the ratio of accelerating gradient to peak surface field, $E_{\mathrm{pk}}/E_{\mathrm{acc}}$, is limited to around 2 [56]. Given the unique geometry of modes in the wagon wheel structure, an effort was made to assess the peak electric fields on the surface of the metallic plates.

Initial simulations of the wagon wheel structure assumed perfect 90-degree corners at the plate edge. While this assumption accurately models the macroscopic behavior of the structure, the calculated fields near the corner are highly mesh-dependent. The peak gradient at the corner calculated by CST eigenmode simulations was observed to scale linearly with mesh density. This is consistent with the discontinuity at a perfect corner that leads to a divergent field [57,58].

The radius of curvature at the corner of the manufactured plates was estimated to be 10 microns after the surface treatment described in the Appendix. Eigenmode simulations of the metamaterial unit cell are unable to mesh corners with radii less than 25 microns, so simulations with larger radii were calculated and fit with the known functional form [57] to estimate the fields at smaller radii. It was determined that all simulations converged at mesh densities greater than 40 cells per wavelength, considered at the 11.7 GHz frequency of interest. The simulated ratio of $E_{\mathrm{pk}}/E_{\mathrm{acc}}$ in the unit cell assuming various corner radii can be seen in blue in Fig. 9.

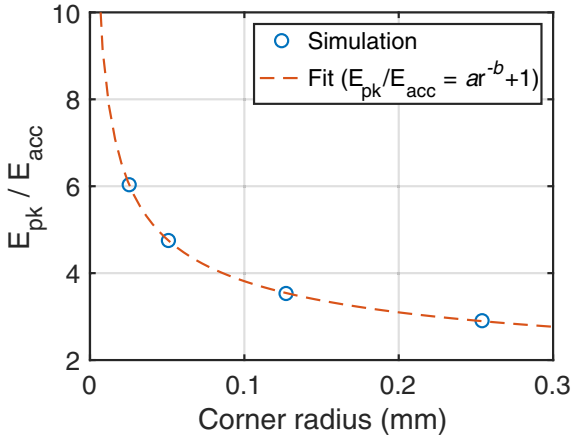

FIG. 9. $E_{\mathrm{pk}}/E_{\mathrm{acc}}$, the ratio of peak surface field to accelerating field, as a function of wagon wheel edge radius.

The functional form of the field near the corner is taken to be $E_{\mathrm{pk}}/E_{\mathrm{acc}} = ar^{-b} + 1$, where a and b are fitting parameters that depend on the geometry being simulated [57]. The fitting parameters take the values $a = 0.991$ and $b = 0.437$. We expect $a \approx 1$ because the fit is for a ratio of fields. From Ref. [57], we expect $1/3 < b < 1/2$ for the 90-degree corner geometry being considered.

Using the fitted function to extrapolate to the estimated corner radius of 10 microns, we estimate $E_{\mathrm{pk}}/E_{\mathrm{acc}} \approx 8.5$ with an uncertainty of about ± 1. For an output power of 500 MW, Eq. (2) calculates that the on-axis accelerating field will reach 130 MV/m. With the field peaking factor of 8.5, peak surface fields are estimated at 1.1 GV/m. This value is above the breakdown field seen in experiments with standard long-pulse (hundreds of ns or longer) accelerator structures. It is known that the breakdown field increases strongly with decreasing pulse width [9,59,60], However, previous results at long pulse cannot be easily scaled to the pulse lengths of 2 ns found in the present experiments. Therefore, the testing of breakdown at high power levels was an important goal of the present research.

Assuming 500 MW of output power, peak magnetic fields of 0.86 MA/m are reached on the outer radius of the spacer plates. This corresponds to a per-pulse temperature increase of 16 K, which is substantially below the accepted per-pulse damage threshold of 40 K [61].

III. COLD TESTS

The fully assembled structure is shown in Fig. 10, with the high-power symmetric combiner in the foreground.

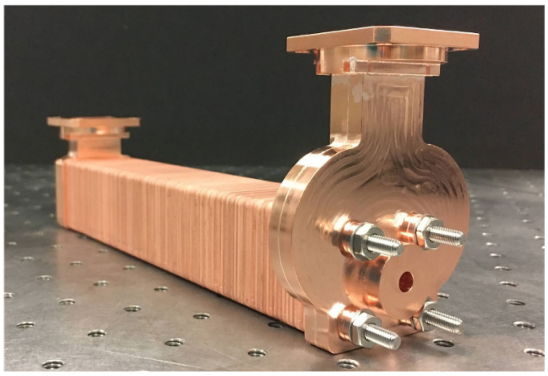

FIG. 10. Assembled Stage III metamaterial power extractor at MIT prior to initial cold tests.

The low-power forward coupler can be seen in the background. A set of four threaded rods compress 100 copper metamaterial cells between the forward and backward couplers. Nuts are tightened against copper-plated steel bushings brazed into the coupler structures to prevent deformation of the internal structure. This design allows for substantial compression to be applied to the structure to maximize plate-to-plate conductivity while maintaining the integrity of the couplers. A jig was designed to enforce the nominal tolerances during assembly. Plate-plate alignment and plate-coupler alignment were maintained to within 25 microns of design.

The structure underwent two sets of cold tests: one at MIT to validate the design and manufacturing, and one after vacuum cleaning and reassembly at AWA prior to beamline tests. The results of the two measurements showed very close agreement, demonstrating the reliability of the assembly process.

The final cold test results prior to beamline installation are presented in Fig. 11. The S_{21} measurement shows less than 0.2 dB of discrepancy between simulation and experiment in the region around the 11.7 GHz interaction frequency. Similarly, the S_{11} results show excellent agreement between simulation and cold test in the expected resonance behavior. These results indicated a successful fabrication and assembly effort.

A beadpull measurement was made at MIT to confirm the dispersion curve of the assembled power extractor [62]. The results in Fig. 12 show that the interaction frequency of the fabricated structure is 11.675 GHz. Although this is 25 MHz lower than the design frequency of 11.7 GHz, it is well within the bandwidth of the structure and within the tunable range of the bunch spacing at AWA. 25 MHz corresponds to a 16 micron dimensional error in manufacturing, which is within the 25 micron tolerance requested. The CST PIC simulation results presented in Sec. V and VI were run for a structure that takes into account these manufacturing shifts and produces an rf output centered at 11.675 GHz. Figure 13 demonstrates the normalized axial electric field amplitude as measured by the beadpull

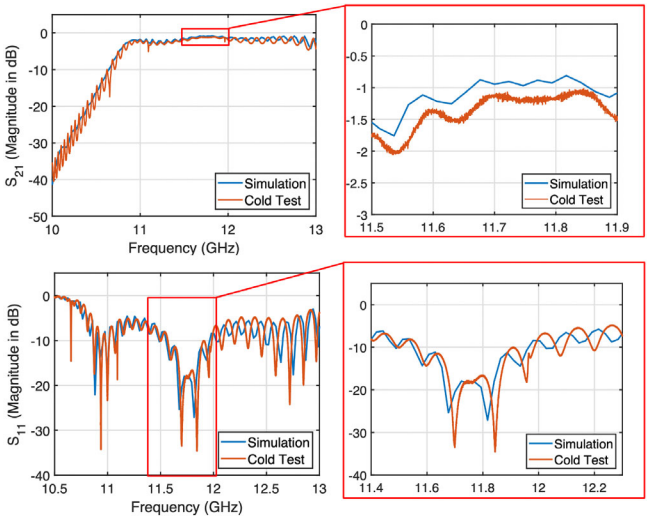

FIG. 11. S-parameters of the assembled structure were measured with a VNA. S_{21} (top) and S_{11} (bottom) show excellent agreement with simulation.

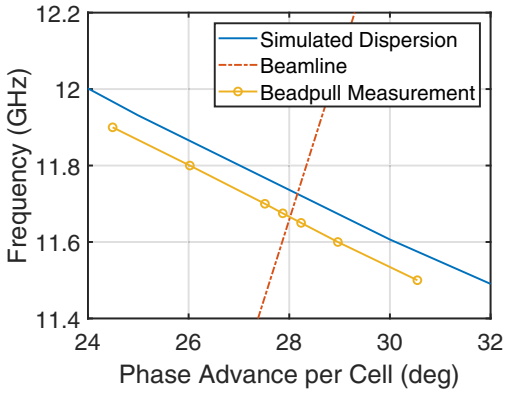

FIG. 12. Simulated dispersion compared to measured dispersion from beadpull cold test. The intersection point with the light line shows the experimental interaction frequency of 11.675 GHz.

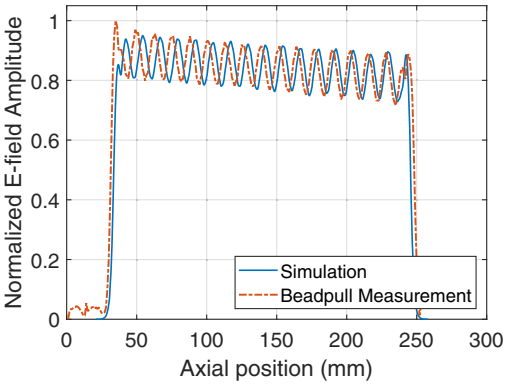

FIG. 13. Simulated (normalized) axial electric field compared to measured values from beadpull experiment at 11.675 GHz.

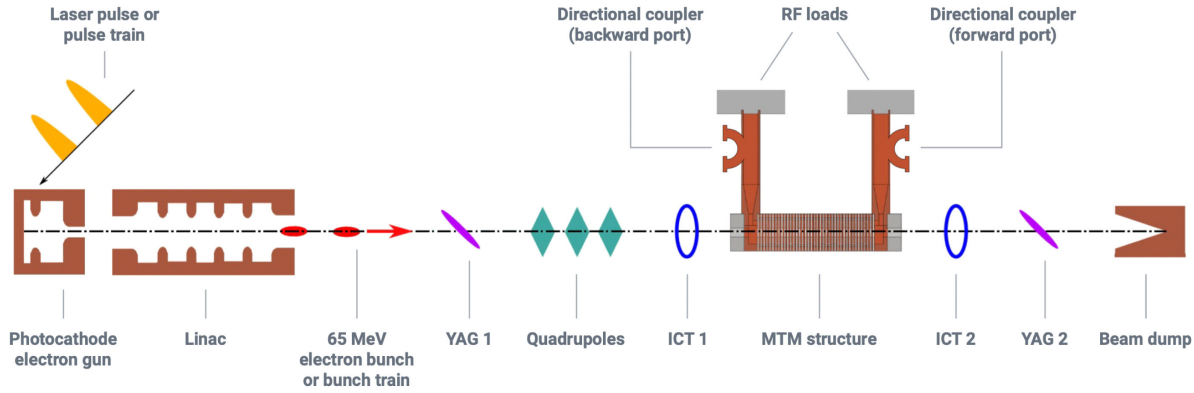

FIG. 14. A simplified model of the AWA beamline setup during the Stage III experimental run. Bunch trains were monitored using YAG screens before and after the structure and charge was measured with ICTs. Dipole trim (not shown) and quadrupole magnets allow for steering. Figure modified from [46].

experiment at 11.675 GHz. The results show an excellent match in field decay over the structure length, α_0, as discussed in Sec. II B.

IV. EXPERIMENTAL SETUP

A simplified schematic of the beamline at the Argonne Wakefield Accelerator is shown in Fig. 14. The electron source is a Cesium telluride photocathode with high quantum efficiency (10%), capable of producing single electron bunches with charge up to 100 nC [63]. The cathode is illuminated by 300 fs pulses from a frequency-tripled Ti-Sapphire laser. A series of beamsplitters allows trains of up to 16 bunches with total charge greater than 600 nC to be generated at the same frequency as the L-band linacs. The bunches are accelerated in six 1.3 GHz cavity accelerators up to 65 MeV. YAG screens can be inserted into the beamline to assist in alignment and diagnostics. A series of steering and quadrupole magnets allow for beam steering and the total charge in a bunch train is measured with integrating current transformers (ICTs).

The Stage III power extractor is installed in a 6-way cross on the beamline, as shown in Fig. 15. The structure is suspended from the output couplers, which transmit output power through the flanges in WR-90 waveguide. The output power from both the forward and backward power extractor ports is sampled with a directional coupler. The output power is then dumped into high power rf loads.

An additional diagnostic feature of this experiment was the inclusion of visible-light diodes for breakdown detection. The setup is shown in Fig. 16. A porous gasket for a 1.33″ CF flange was designed for at least 50 dB of attenuation at 11.7 GHz to avoid any possibility of breakdown at the quartz window. A collimator located directly outside the window focuses light into a fiber optic cable. The collimator and output window are enclosed in a dark box to lower background noise. A FPD610-FC-VIS diode detector from Menlo Systems with a gain of $\sim 10^6$ V/W and rise time of 1 ns was used to convert the signal from the fiber optic to an oscilloscope-readable voltage. Although designed specifically for this experiment, this detection system was previously used to successfully sample breakdown events on a high-power *X*-band electron gun test at AWA [64].

Two Tektronix oscilloscopes were used in the experiment. A model with 8 GHz bandwidth was used to sample the ICT signals in order to measure the bunch charge. A 23 GHz model was used to directly sample the 11.7 GHz output traces and the diode signals. The data from each oscilloscope was captured on a PC using a custom

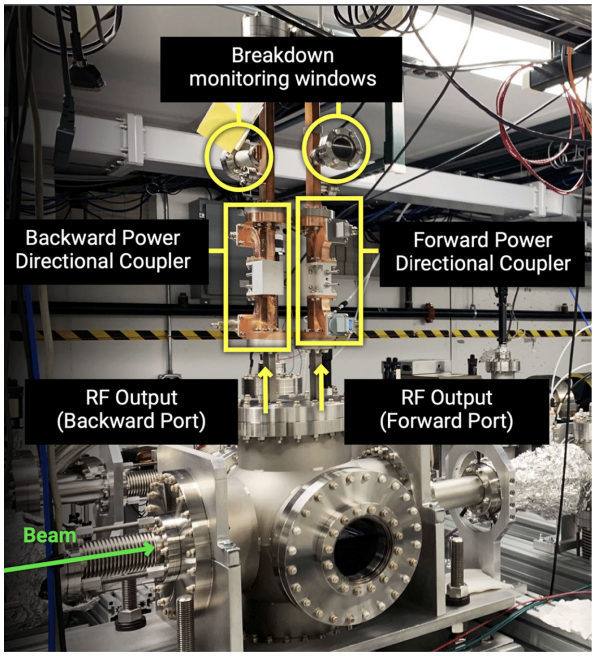

FIG. 15. Vacuum chamber in which the power extractor was installed on the AWA beamline. Both the high power and low power rf output waveguides were sampled with a directional coupler and breakdown-detection diodes (not shown), with the power absorbed by rf loads at the end of the waveguide.

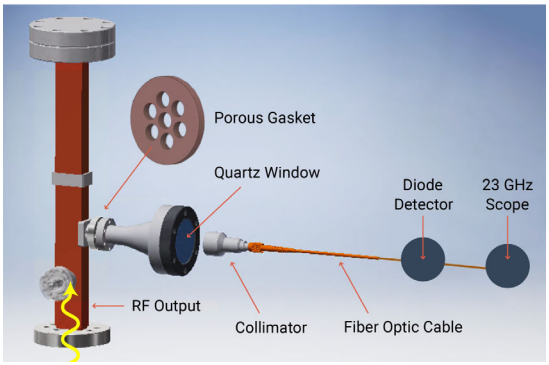

FIG. 16. Schematic of breakdown detection system. A spare 1.33″ port in the output waveguides is fitted with a taper, separated by a porous gasket to reject rf leakage. The collimator outside the window picks up light and focuses into a fiber optic cable. The light is detected by a fast diode detector and monitored on an oscilloscope.

MATLAB script, which provided real-time power and charge measurements.

V. LOW POWER RESULTS

Low charge single bunches and bunch trains were used to test the electromagnetic properties of the structure and agreement with theory before pushing to high power. Figure 17 shows the excellent agreement between experiment and CST PIC simulation for the output power generated by a single 7 nC bunch. The flat-top power level matches closely, as does the pulse width. A Fourier transform of this output pulse can be seen in Fig. 18, which also shows excellent agreement.

Figure 19 compares simulation and experiment for a train of eight bunches with 12 nC total charge. The close agreement demonstrates that the structure correctly allows for the coherent addition of radiation from multiple bunches. The frequency spectrum of this pulse, shown in Fig. 20, shows both the correct interaction frequency as well as the expected bandwidth reduction relative to the single bunch case.

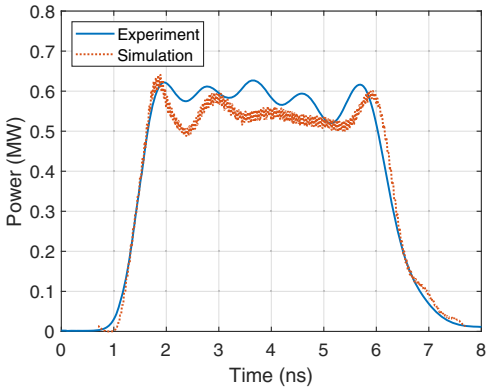

FIG. 17. Experimental rf pulse generated by a single 7 nC bunch, along with accompanying PIC simulation results.

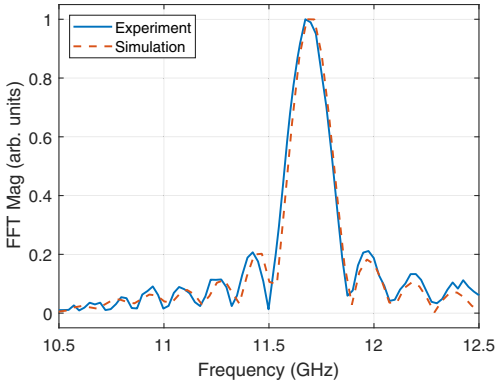

FIG. 18. FFT of the rf pulse in Fig. 17 from a single 7 nC bunch and accompanying PIC simulation results.

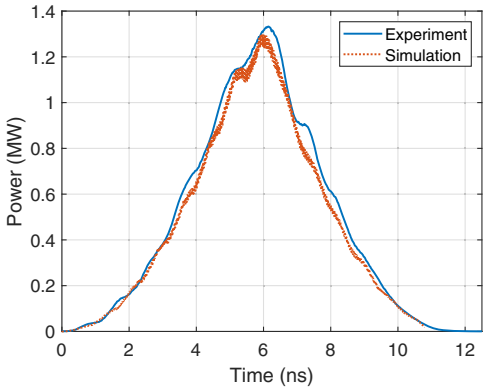

FIG. 19. Rf Pulse of a eight bunch train with total charge of 12 nC, along with accompanying PIC simulation results.

VI. HIGH POWER RESULTS

After establishing that the structure behaves as expected with low charge bunches, two high charge experimental

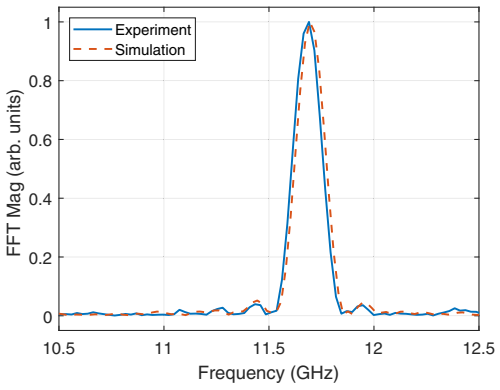

FIG. 20. FFT of the rf pulse in Fig. 19 from an eight bunch train with total charge of 12 nC bunch, along with accompanying PIC simulation results.

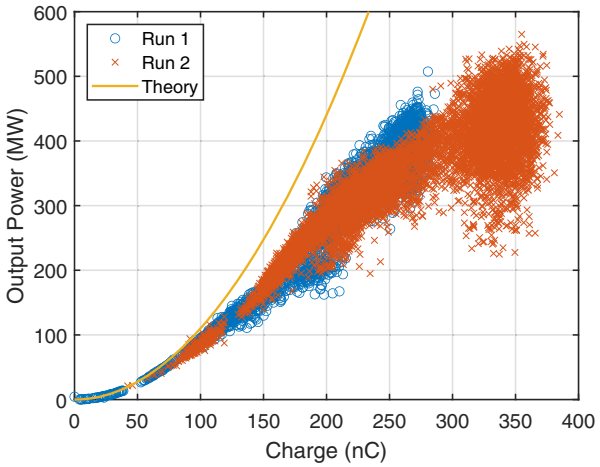

FIG. 21. Plot of output power vs incident charge for a sample of 600 experimental shots from Run 1 and Run 2 compared to theory. The deviation from theory starts to appear above 100 nC of total charge.

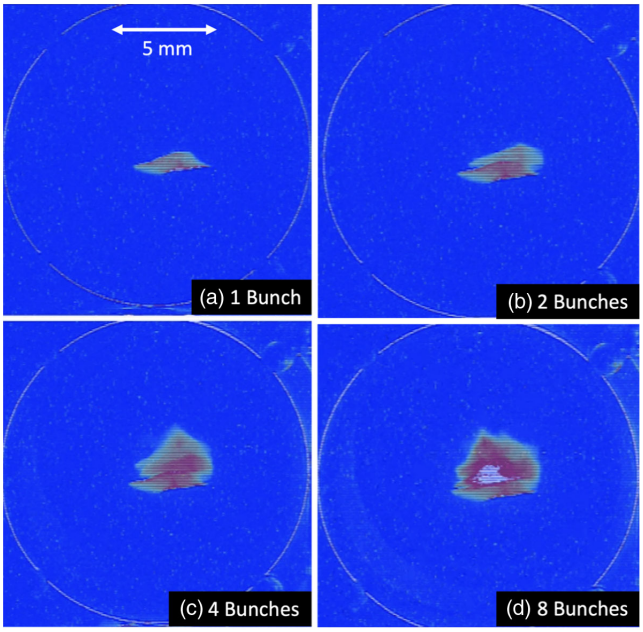

FIG. 22. YAG images taken before (upstream from) the power extractor show an bunch-to-bunch offset that is on the order of the bunch diameter. This is believed to be due to undamped transverse wakes in the linear accelerator. The total charge in this bunch train is 230 nC.

runs were undertaken with the Stage III experiment. Run 1 was completed in February 2021 and Run 2 was completed in October 2021. During Run 1, approximately 20k shots were collected and a maximum charge of 280 nC in an eight bunch train was available from the AWA beamline. During Run 2, approximately 10k shots were collected and improvements to the AWA laser system increased the maximum available charge to 380 nC. A plot of output power versus bunch charge for both experimental runs is shown in Fig. 21, along with the expected trend from theory. The large spread in output power generated from bunch trains with 300–380 nC of total charge during Run 2 was caused by a different beam alignment strategy employed to maximize the generated output power.

It can be seen from Fig. 21 that the output power generated by the Stage III experiment begins to deviate from the theoretical value above around 100 nC. YAG screens located two quadrupole magnets upstream from the structure revealed that as the total charge in the train was increased beyond this level, bunches 2 through 8 began to shift relative to the initial bunch. This can be seen in an example set of YAG images in Fig. 22, in which the later bunches shift vertically by several millimeters. This behavior was highly dependent upon the beamline conditions, and the direction of bunch shifting varied. Because these images were taken upstream from the power extractor, this effect must be due to some feature of the AWA beamline itself, either during beam acceleration or transport, rather than the metamaterial structure. The most likely cause of the shifting is believed to be undamped transverse wakes in the 65 MeV linear accelerators.

This bunch-to-bunch shift and accompanying angle in the beam trajectory may not be detrimental to the performance of power extractors with larger beam tunnels and lower shunt impedance. The 6 mm diameter beam tunnel gives the wagon wheel MTM the advantage of higher power generation efficiency (as does the high group velocity of the structure), but also makes it more prone to interception of bunches traveling off axis. As a result, the transmission of the full eight bunch train through the structure was challenging at higher total charge.

An attempt was made to simulate the effect of an off-axis and angled beam on the rf output from the MTM structure. Replicating the specific condition of the bunch trains as they entered the structure in experiment was made difficult by limitations of the YAG data. As mentioned, the YAG screen that produced the images in Fig. 22 is located before two quadrupole magnets that focus the beam prior to entering the structure. In addition, the YAG screen images only show a measure of position, not trajectory. To try to characterize the bunch behavior, an extensive set of PIC simulations were run with a wide array of assumptions. Simulations which assume that bunches 2-8 possessed trajectories that were shifted and tilted by an amount linearly increasing with bunch number were found to match experimental results. This is consistent with the belief that this bunch behavior is caused by undamped transverse wakes in the linac, the effect of which we would expect to increase linearly with bunch number.

With the stated assumptions regarding the incident bunch trajectory, the experimental rf output waveform from high-charge eight bunch trains can be successfully simulated. A representative experimental output trace from a 224 nC eight bunch train can be seen in solid blue in

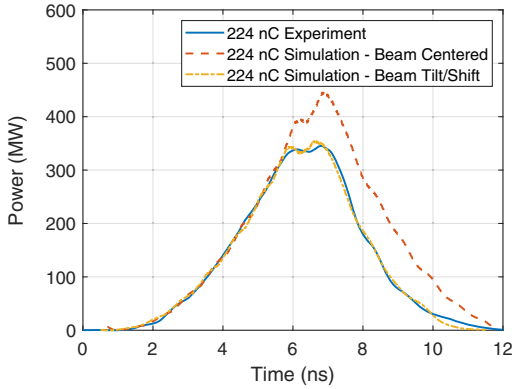

FIG. 23. Experimental plot of typical 350 MW experimental trace in solid blue, from a 224 nC 8-bunch train. The red dashed simulation assumes an 224 nC eight-bunch train that centered on-axis. The yellow dot-dashed simulation assumes the same bunch train but offset by 0.05 mm per bunch and tilted by 0.025° per bunch.

Fig. 23. The output pulse expected from a 224 nC train of eight bunches centered on axis is represented by the dashed red simulation plot. It can be seen that the seventh and eighth bunches do not contribute substantially to the rf output in the experiment. The yellow dot-dashed line in Fig. 23, which closely matches the experimental trace, assumes an eight-bunch train of total charge 224 nC with the first bunch on axis and subsequent bunches offset by 0.05 mm/bunch and tilted by 0.025°/bunch.

The highest power generated during Run 1 can be seen in Fig. 24, in which 510 MW was generated in a 2.1 ns pulse (FWHM) from an eight bunch train with 280 nC of total charge. Simulations assuming a shift of 0.25 mm/bunch and a tilt 0.12°/bunch closely match experimental data. Due to the offset, the contribution of the eighth bunch is almost entirely lost.

The highest power generated during Run 2 is shown in Fig. 25, in which 565 MW of output power was generated

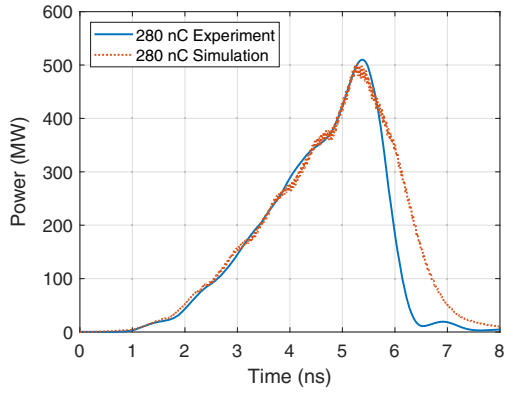

FIG. 24. Experimental trace showing 510 MW of generated output power at 11.7 GHz. The charge measured before entering the structure was 280 nC. The red simulation assumes the bunch train is offset by 0.25 mm per bunch and tilted by 0.12° per bunch.

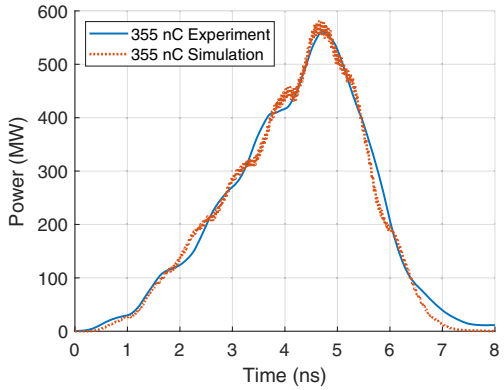

FIG. 25. Experimental trace showing 565 MW of generated output power at 11.7 GHz. The charge measured before entering the structure was 355 nC. The red simulation assumes the bunch train is offset by 0.3 mm per bunch and tilted by 0.21° per bunch.

from an eight bunch train with total charge 355 nC. The pulse width is 2.7 ns. This represents the highest power generated by a power extractor to date at the Argonne Wakefield Accelerator facility. If applied in a collinear wakefield accelerator configuration, this power level corresponds to an on-axis accelerating field of more than 135 MV/m. Simulations assuming a shift of 0.3 mm/bunch and a tilt of 0.21°/bunch match well with the experimental trace. In this shot, the contribution of both the seventh and eighth bunch is negligible.

It is important to note that these simulations do not take into account the true emittance values of the experimental bunch, which was not measured in real time. The result of including this emittance in a more advanced PIC code would likely change the necessary bunch offset/tilt values required to replicate the experimental results.

No evidence of breakdown was observed during either Run 1 or Run 2. The highest surface field obtained for the 565 MW output power pulse is estimated to be 1.15 GV/m. The absence of breakdown is supported by two experimental measurements. First, there were no signals on the visible light diode detectors that could be attributable to breakdown events. Second, no shots were observed in which unexpected reflected power was measured at the low power forward port. If breakdowns were to have occurred in the beam tunnel to the extent that they were responsible for the pulse shortening observed in Figs. 24 and 25, it is expected that substantial power would be reflected toward the forward coupler.

VII. DISCUSSION AND CONCLUSIONS

Up to 565 MW of output power at 11.7 GHz has been generated using a metamaterial-based power extractor for structure-based wakefield acceleration. This represents the highest power generated at the Argonne Wakefield Accelerator facility to date. These results were enabled in part by the reduction of rf loss in the structure over the

previous Stage I/II experiments by replacing steel components with copper. The copper parts were processed to smooth sharp edges and surface defects. No breakdown events were observed either from visible light diagnostics or from power reflected within the structure. The development of a symmetric high-power output coupler and power combiner reduced transverse deflecting fields by almost two orders of magnitude, making power generation more efficient and increasing ease of bunch transmission.

At the power levels achieved, the lack of breakdown observation indicates that the surface etching treatment was sufficient to avoid breakdown during the short, 2.7 ns rf pulses. However, the estimated field peaking factor of 8.5 is still substantial. Future iterations of the experiment may seek to utilize a more substantial plate processing method than that described in the Appendix, such as electropolishing, to achieve a larger corner radius after EDM machining.

Simulations consistent with the experimental results in this paper show that power levels over one gigawatt would be generated by a train of eight bunches with 360 nC of total charge at AWA under the condition that bunches transit the structure on-axis. Efforts currently underway at the AWA to improve electron beam quality and alignment should allow for future experimental demonstration at the GW power level [65,66].

ACKNOWLEDGMENTS

This research was supported by the U.S. Department of Energy, Office of Science, Office of High Energy Physics under Award No. DE-SC0015566. The work at the AWA was funded through the U.S. Department of Energy, Office of Science under Contract No. DE-AC02-06CH11357.

APPENDIX: METAMATERIAL PLATE SURFACE TREATMENT

As discussed in Sec. II B, the propensity of copper to incur surface damage during manufacturing and handling was a primary reason that the structure plates were manufactured from stainless steel in the Stage I/II experiments. Although the surface damage was substantially mitigated by careful handling procedures, there were still residual surface defects from manufacturing. An example of this damage can be seen in Fig. 26(a). Without removing these sharp features, they would likely act as breakdown initiation sites during the high power testing of the structure. A similar concern also existed for the sharp edges naturally formed by the EDM manufacturing process.

A systematic study was undertaken to investigate the use of Citranox, a citric acid solution, to remove these sharp surface features and reduce the risk of breakdown during experiment. Citranox was chosen because it is a standard chemical used in vacuum preparation at the AWA facility, and hence raises no vacuum cleanliness concerns. The plates were mounted in a custom mount that holds 50 plates

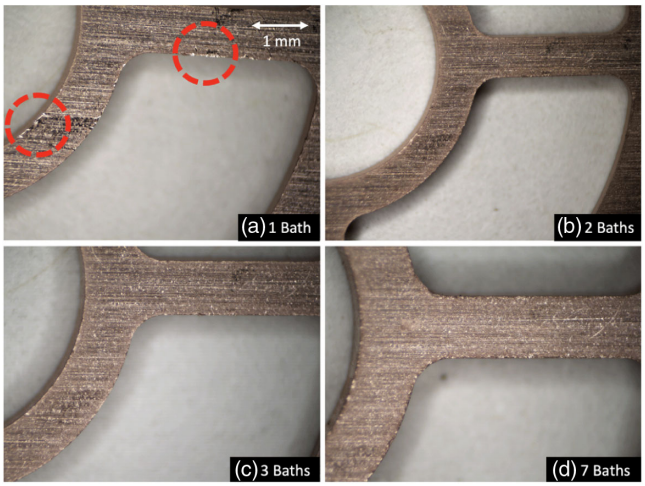

FIG. 26. Comparison of plate surface finish after one, two, three, and seven baths. Surface damage, circled, is clearly visible after a single 2% Citranox bath. While two baths still leave obvious surface defects, plates started to exhibit noticeable pitting after more than four baths (seven bath case is shown for clarity).

at a time. The jig was placed within a 1 L beaker and fully submerged in 35°C Citranox solution. The concentration of the solution was 2% for the first bath and 5% for all subsequent baths. The beaker was then placed into a sonicator. After a period of 15 minutes, the plates were rotated and sonicated for an additional 15 minutes. After the 30 minute Citranox sonication, the plates were rinsed with water and then with acetone.

After the first bath, the damaged regions are still clearly visible. With successive baths, the damaged regions become less prominent, see Figs. 26(b) and 26(c). After 7 baths, irregular corner pitting becomes visible, as seen in

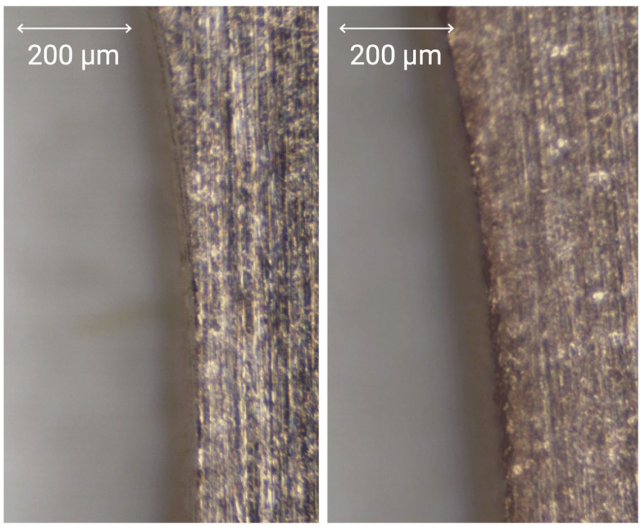

FIG. 27. Visible microscope images of the edges of plates before (left) and after (right) treatment with Citranox bath procedure. Edges are visibly rounded by the process.

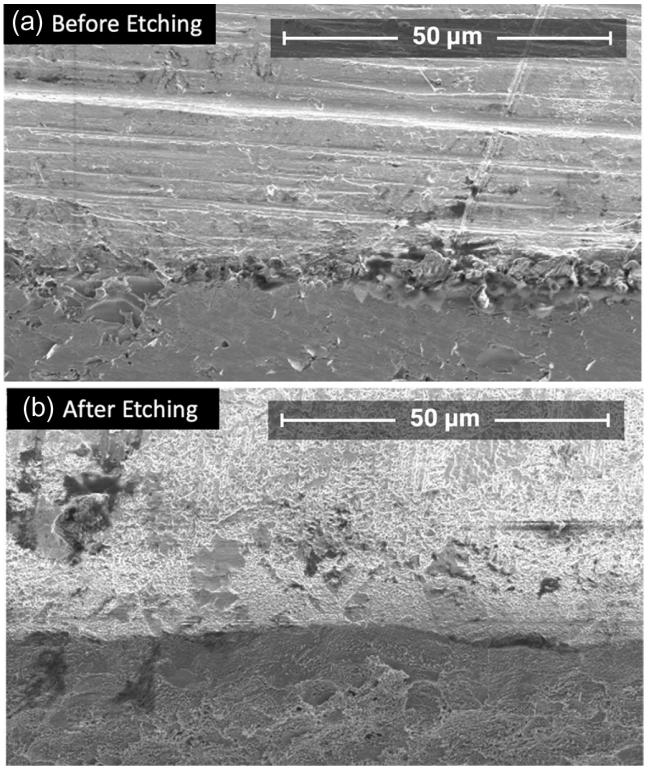

FIG. 28. (*Angled View*) Scanning electron microscope images of the plate edge from before (top) and after (bottom) Citranox treatment.

Fig. 26(d). Four baths were chose as the optimal number to remove sharp features while minimizing excessive pitting.

A visible microscope before/after comparison of the four-bath etching process can be seen in Fig. 27, in which the corner of the plate was rounded by the procedure. Sample plates were sent for SEM analysis to validate the visual results. Images taken of the plate edge from a 45-degree perspective are shown in Fig. 28. The ragged edge left by the EDM manufacturing at top was smoothed by the etching process, leaving the more consistent edge seen at bottom with peaking features removed.

It was important to ensure that this etching process does not change the nominal dimensions of the structure plates, which may change the resonance features of the power extractor after assembly. During the initial process calibration, the dimensions of several plates were measured using a micrometer over the course of seven baths. Despite the clear effects on the corner features, nominal dimensional changes were limited to less than 10 microns after seven baths, which is substantially less than the machining tolerance of ± 25 um. After four baths, the nominal dimensional changes to the plates were below the measurement threshold.

[1] E. R. Colby and L. K. Len, Rev. Accel. Sci. Techol. **09**, 1 (2016).

[2] T. Antonsen *et al.*, Advanced Accelerator Development Strategy Report: DOE Advanced Accelerator Concepts Research Roadmap Workshop, Technical Report, 2016, 10.2172/1358081.

[3] B. Cros and P. Muggli, Towards a proposal for an advanced linear collider report on the advanced and novel accelerators for high energy physics roadmap workshop, CERN, Geneva, Technical Report, 2017, http://cds.cern.ch/record/2298632.

[4] E. I. Simakov, V. A. Dolgashev, and S. G. Tantawi, Nucl. Instrum. Methods Phys. Res., Sect. A **907**, 221 (2018).

[5] T. Higo, Report from kek (high gradient study results from nextef), arXiv:1203.3626.

[6] V. Dolgashev, S. Tantawi, Y. Higashi, and B. Spataro, Appl. Phys. Lett. **97**, 171501 (2010).

[7] A. D. Cahill, J. B. Rosenzweig, V. A. Dolgashev, S. G. Tantawi, and S. Weathersby, Phys. Rev. Accel. Beams **21**, 102002 (2018).

[8] M. A. K. Othman, J. Picard, S. Schaub, V. A. Dolgashev, S. M. Lewis, J. Neilson, A. Haase, S. Jawla, B. Spataro, R. J. Temkin, S. Tantawi, and E. A. Nanni, Appl. Phys. Lett. **117**, 073502 (2020).

[9] A. Grudiev, S. Calatroni, and W. Wuensch, Phys. Rev. ST Accel. Beams **12**, 102001 (2009).

[10] W. Gai, P. Schoessow, B. Cole, R. Konecny, J. Norem, J. Rosenzweig, and J. Simpson, Phys. Rev. Lett. **61**, 2756 (1988).

[11] C. Jing, A. Kanareykin, J. Power, M. Conde, Z. Yusof, and W. Gai, AIP Conf. Proc. **877**, 511 (2006).

[12] F. Gao, M. E. Conde, W. Gai, C. Jing, R. Konecny, W. Liu, J. G. Power, T. Wong, and Z. Yusof, Phys. Rev. ST Accel. Beams **11**, 041301 (2008).

[13] C. Jing, A. Kanareykin, J. G. Power, M. Conde, W. Liu, S. Antipov, P. Schoessow, and W. Gai, Phys. Rev. Lett. **106**, 164802 (2011).

[14] G. Andonian, D. Stratakis, M. Babzien, S. Barber, M. Fedurin, E. Hemsing, K. Kusche, P. Muggli, B. O'Shea, X. Wei, O. Williams, V. Yakimenko, and J. B. Rosenzweig, Phys. Rev. Lett. **108**, 244801 (2012).

[15] S. Antipov, C. Jing, A. Kanareykin, J. E. Butler, V. Yakimenko, M. Fedurin, K. Kusche, and W. Gai, Appl. Phys. Lett. **100**, 132910 (2012).

[16] W. Gai, J. G. Power, and C. Jing, J. Plasma Phys. **78**, 339 (2012).

[17] B. D. O'Shea, G. Andonian, S. K. Barber, K. L. Fitzmorris, S. Hakimi, J. Harrison, P. D. Hoang, M. J. Hogan, B. Naranjo, O. B. Williams, V. Yakimenko, and J. B. Rosenzweig, Nat. Commun. **7**, 12763 (2016).

[18] D. Wang, S. Antipov, C. Jing, J. G. Power, M. Conde, E. Wisniewski, W. Liu, J. Qiu, G. Ha, V. Dolgashev, C. Tang, and W. Gai, Phys. Rev. Lett. **116**, 054801 (2016).

[19] C. Jing, Rev. Accel. Sci. Techol. **09**, 127 (2016).

[20] Q. Gao, G. Ha, C. Jing, S. P. Antipov, J. G. Power, M. Conde, W. Gai, H. Chen, J. Shi, E. E. Wisniewski, D. S. Doran, W. Liu, C. E. Whiteford, A. Zholents, P. Piot, and S. S. Baturin, Phys. Rev. Lett. **120**, 114801 (2018).

[21] K. Lekomtsev, A. Aryshev, A. A. Tishchenko, M. Shevelev, A. Lyapin, S. Boogert, P. Karataev, N. Terunuma, and J. Urakawa, Phys. Rev. Accel. Beams **21**, 051301 (2018).

[22] C. Jing, S. Antipov, M. Conde, W. Gai, W. Lui, N. Neveu, J. G. Power, J. Qiu, D. Wang, and E. Wisniewski, Nucl. Instrum. Methods Phys. Res. A **898**, 72 (2018).

[23] J. Shao, C. Jing, E. Wisniewski, G. Ha, M. Conde, W. Liu, J. Power, and L. Zheng, Phys. Rev. Accel. Beams **23**, 011301 (2020).

[24] M. Dal Forno, V. Dolgashev, G. Bowden, C. Clarke, M. Hogan, D. McCormick, A. Novokhatski, B. O'Shea, B. Spataro, S. Weathersby, and S. G. Tantawi, Phys. Rev. Accel. Beams **19**, 111301 (2016).

[25] M. Aicheler, P. Burrows, M. Draper, T. Garvey, P. Lebrun, K. Peach, N. Phinney, H. Schmickler, D. Schulte, and N. Toge, *A Multi-TeV Linear Collider Based on CLIC Technology: CLIC Conceptual Design Report*, CERN Yellow Reports: Monographs (CERN, Geneva, 2012).

[26] H. Zha and A. Grudiev, Phys. Rev. Accel. Beams **20**, 042001 (2017).

[27] C. Jing, S. Antipov, A. Kanareykin, P. Schoessow, M. Conde, W. Gai, and J. Power, in *4th International Particle Accelerator Conference* (JACoW, Geneva, 2013).

[28] M. S. Ricardo Marques and Ferran Martin, *Metamaterials with Negative Parameters* (John Wiley and Sons, New York, 2008).

[29] H. Chen and M. Chen, Mater. Today **14**, 34 (2011).

[30] S. Xi, H. Chen, T. Jiang, L. Ran, J. Huangfu, B.-I. Wu, J. A. Kong, and M. Chen, Phys. Rev. Lett. **103**, 194801 (2009).

[31] Z. Duan, X. Tang, Z. Wang, Y. Zhang, X. Chen, M. Chen, and Y. Gong, Nat Commun. **8**, 14901 (2017).

[32] J. S. Hummelt, X. Lu, H. Xu, I. Mastovsky, M. A. Shapiro, and R. J. Temkin, Phys. Rev. Lett. **117**, 237701 (2016).

[33] X. Lu, J. C. Stephens, I. Mastovsky, M. A. Shapiro, and R. J. Temkin, Phys. Plasmas **25**, 023102 (2018).

[34] Z. Duan, M. A. Shapiro, E. Schamiloglu, N. Behdad, Y. Gong, J. H. Booske, B. N. Basu, and R. J. Temkin, IEEE Trans. Electron Devices **66**, 207 (2019).

[35] J. W. Luginsland, J. A. Marshall, A. Nachman, and E. Schamiloglu, *High power microwave sources and technologies using metamaterials* (Wiley-IEEE Press, New York, 2021).

[36] T. Rowe, N. Behdad, and J. H. Booske, IEEE Trans. Plasma Sci. **44**, 2476 (2016).

[37] S. Antipov, L. Spentzouris, W. Liu, W. Gai, and J. G. Power, J. Appl. Phys. **102**, 034906 (2007).

[38] S. Antipov, L. Spentzouris, W. Gai, M. Conde, F. Franchini, R. Konecny, W. Liu, J. G. Power, Z. Yusof, and C. Jing, J. Appl. Phys. **104**, 014901 (2008).

[39] E. I. Smirnova, A. S. Kesar, I. Mastovsky, M. A. Shapiro, and R. J. Temkin, Phys. Rev. Lett. **95**, 074801 (2005).

[40] E. I. Smirnova, I. Mastovsky, M. A. Shapiro, R. J. Temkin, L. M. Earley, and R. L. Edwards, Phys. Rev. ST Accel. Beams **8**, 091302 (2005).

[41] E. I. Simakov, S. A. Arsenyev, C. E. Buechler, R. L. Edwards, W. P. Romero, M. Conde, G. Ha, J. G. Power, E. E. Wisniewski, and C. Jing, Phys. Rev. Lett. **116**, 064801 (2016).

[42] M. Peng *et al.*, in *10th International Particle Accelerator Conference* (JACoW, Geneva, 2019), pp. 734–737.

[43] J. Shao, M. Conde, D. Doran, C.-J. Jing, and J. Power, in *Proc. 9th International Particle Accelerator Conference (IPAC'18), Vancouver, BC, Canada, April 29-May 4, 2018*, International Particle Accelerator Conference No. 9 (JACoW Publishing, Geneva, Switzerland, 2018), pp. 1539–1541.

[44] P. Zou, L. Xiao, X. Sun, W. Gai, and T. Wong, J. Appl. Phys. **90**, 2017 (2001).

[45] C. Jing, A. Kanareykin, S. Kazakov, W. Liu, E. Nenasheva, P. Schoessow, and W. Gai, Nucl. Instrum. Methods Phys. Res., Sect. A **594**, 132 (2008).

[46] X. Lu, M. A. Shapiro, I. Mastovsky, R. J. Temkin, M. Conde, J. G. Power, J. Shao, E. E. Wisniewski, and C. Jing, Phys. Rev. Lett. **122**, 014801 (2019).

[47] X. Lu, J. F. Picard, M. A. Shapiro, I. Mastovsky, R. J. Temkin, M. Conde, J. G. Power, J. Shao, E. E. Wisniewski, M. Peng, G. Ha, J. Seok, S. Doran, and C. Jing, Appl. Phys. Lett. **116**, 264102 (2020).

[48] F. Falcone, T. Lopetegi, M. A. G. Laso, J. D. Baena, J. Bonache, M. Beruete, R. Marqus, F. Martn, and M. Sorolla, Phys. Rev. Lett. **93**, 197401 (2004).

[49] T. P. Wrangler, *RF Linear Accelerators*, 2nd ed. (Wiley-VCH, New York, 2008).

[50] Z. Duan, M. A. Shapiro, E. Schamiloglu, N. Behdad, Y. Gong, J. H. Booske, B. N. Basu, and R. J. Temkin, IEEE Trans. Electron Devices **66**, 207 (2019).

[51] X. Lu, Metamaterial structures for wakefield acceleration and high power microwave generation, Ph.D. thesis, Massachusetts Institute of Technology, Department of Physics, 2019.

[52] J. Picard, High power microwave generation for advanced particle acceleration, Ph.D. thesis, Massachusetts Institute of Technology, Department of Physics, 2022.

[53] M. Peng, Short pulse high power test study of high-gradient accelerating structure, Ph.D. thesis, Tsinghua University, 2021.

[54] J. Shi, H. Chen, Q. Gao, X. Wu, Y. Yang, H. Zha, W. Gai, and C. Jing, in *4th International Particle Accelerator Conference* (JACoW, Geneva, 2013), pp. 2771–2773.

[55] Z. Li, L. D. Bentson, J. Chan, D. H. Dowell, C. Limborg-Deprey, J. F. Schmerge, D. C. Schultz, and L. Xiao, Report No. SLAC-PUB-11728, 2006.

[56] F. Gerigk, Cavity types, arXiv:1111.4897.

[57] L. Krähenbühl, F. Buret, R. Perrussel, D. Voyer, P. Dular, V. Péron, and C. Poignard, Numerical treatment of rounded and sharp corners in the modeling of 2D electrostatic fields, J. Microw. Optoelectron. Electromagn. Appl. **10**, 66 (2011).

[58] J. Van Bladel, IEEE Trans. Antennas Propag. **33**, 450 (1985).

[59] W. Wuensch, C. Achard, S. Dobert, H. Braun, I. Syratchev, M. Taborelli, and I. Wilson, in *Proceedings of the 2003 Particle Accelerator Conference, Vol. 1* (IEEE, New York, 2003), pp. 495–497, Vol. 1.

[60] A. D. Cahill, J. B. Rosenzweig, V. A. Dolgashev, S. G. Tantawi, and S. Weathersby, Phys. Rev. Accel. Beams **21**, 102002 (2018).

[61] B. J. Munroe, Experimental studies of novel accelerator structures at 11 GHz and 17 GHz, Ph.D. thesis, Massachusetts Institute of Technology, 2016.

[62] C. Steele, A nonresonant perturbation theory, IEEE Trans. Microw. Theory Tech. **14**, 70 (1966).

[63] E. Wisniewski, S. Antipov, M. Conde, D. Doran, W. Gai, C. Jing, W. Liu, J. Power, and C. Whiteford, in

6th International Particle Accelerator Conference (JACoW, Geneva, 2015), pp. 3283–3285.

[64] J. H. Shao, D. S. Doran, W. Liu, J. G. Power, E. W. C. Whiteford, C. J. Jing, S. V. Kuzikov, X. Lu, P. Piot, and W. H. Tan, in *12th International Particle Accelerator Conference* (JACoW, Geneva, 2021), THPAB331.

[65] W. Liu, J. M. Byrd, D. S. Doran, A. N. J. G. Ha, P. Piot, J. G. Power, J. H. Shao, G. Shen, C. Whiteford, and E. E. Wisniewski, in *12th International Particle Accelerator Conference* (JACoW, Geneva, 2021), TUPAB295.

[66] W. Liu, D. S. Doran, G. Ha, P. Piot, J. G. Power, J. H. Shao, C. Whiteford, E. E. Wisniewski, L. R. Doolittle, D. Filippetto, D. Li, S. Paiagua, C. Serrano, and V. K. Vytla, in *12th International Particle Accelerator Conference* (JACoW, Geneva, 2021), TUPAB296.